Available online at www.sciencedirect.com
SCIENCE DIRECT®
International Journal of Heat and Mass Transfer 48 (2005) 4041–4061
International Journal of HEAT and MASS TRANSFER
www.elsevier.com/locate/ijhmt

Coalescence of colliding van der Waals liquid drops

Yasmin Meleán [a], Leonardo Di G. Sigalotti [b,*]

[a] Laboratoire de Tectonophysique, Université de Montpellier II, 34095 Montpellier Cedex 05, France
[b] Centro de Física, Instituto Venezolano de Investigaciones Científicas, IVIC, Apartado Postal 21827, Caracas 1020A, Venezuela

Received 22 October 2004; received in revised form 31 March 2005
Available online 29 June 2005

Abstract

Here, we present two-dimensional numerical calculations of the head-on and off-centre binary collision dynamics of equal-sized, van der Waals liquid drops using the method of smoothed particle hydrodynamics (SPH). Because of the planar geometry used to represent the drops, the simulations apply to the collision of two infinitely long cylinders. The outcome of coalescence, in which two drops combine permanently, is studied only for low energy impact collisions with Reynolds (Re) and Weber (We) numbers in the ranges $23 \leqslant Re \leqslant 68$ and $1 \leqslant We \leqslant 10$, respectively. In particular, the effects of varying both the impact velocity and the impact parameter on the outcome of permanent coalescence are investigated.

Keywords: Fluid dynamics; Numerical-methods; Viscosity-liquids; Drops and bubbles; van der Waals-molecules

1. Introduction

The phenomenon of binary coalescence, in which two liquid drops combine and generate one single drop via an inelastic collision, is an essential feature in many industrial and natural processes and therefore its prediction and control is of great practical importance. For instance, many applications of interest to chemical engineers include liquid–liquid extraction, emulsification, spray coating, hydrocarbon fermentation and waste treatment [1–3]. In particular, the coalescence of oil drops is relevant to many industrial and environmental clean-up operations. The success of liquid–liquid extraction operations depends on the subsequent coalescence of the dispersed drops which have deliberately been formed to enhance the rate of mass transfer [4]. Moreover, the coalescence of the emulsions formed during alkaline flooding operations is necessary to produce a stable oil bank and achieve enhanced oil recovery. In the petroleum refineries, coalescence of fine oil mist is attained using porous coalescers, settlers, chemicals and electric fields to break up the emulsions. The collision and coalescence of liquid drops in Diesel engine sprays is also of great interest because coalescence affects the size of the drops in the engine cylinder, which in turn may affect its performance and emission characteristics [3]. Also, the coalescence of liquid drops plays a fundamental role in metereological studies of raindrop and precipitation formation in warm-based and maritime clouds [5], and in processing of food products and other emulsions.

When a pair of drops collide in a gas–liquid or liquid–liquid dispersion, the interfaces separating the drops from the continuous phase distort to form a flat

* Corresponding author. Tel.: +58 0212 5041369; fax: +58 0212 5041148.
E-mail addresses: melean@msem.univ-montp2.fr (Y. Meleán), lsigalot@cassini.ivic.ve (L. Di G. Sigalotti).

0017-9310/$ - see front matter © 2005 Elsevier Ltd. All rights reserved.
doi:10.1016/j.ijheatmasstransfer.2005.04.006

lamella, which must drain to a certain critical thickness before it finally ruptures leading to coalescence [6–8]. The rate of film drainage will then determine the rate of coalescence. Because of its complexity, the study of this three-dimensional (3D) free-surface flow has been mostly limited to experiments of controlled collisions between pairs of drops in free flight. Extensive experimental investigation of the binary collision dynamics of water and fuel droplets can be found in the literature for a range of drop size ratios, Reynolds numbers, Weber numbers and impact parameters [9–14]. It is generally accepted that when two drops collide, there are several possible outcomes, depending on the kinetic energy of the collision, the sizes of the impinging drops, the impact parameter and the fluid properties. All these factors can be parametrized in terms of the dimensionless Reynolds number (Re), Weber number (We) and impact parameter (χ), which for equal-sized drops are defined as

$$Re = \frac{\rho v_{\rm rel} D}{\eta}, \quad We = \frac{\rho v_{\rm rel}^2 D}{\sigma}, \quad \chi = \frac{X}{D}, \tag{1}$$

where ρ, η and σ designate the density, shear viscosity and surface tension of the drop fluid, respectively, $v_{\rm rel}$ is the relative velocity of the colliding drops, D is their diameter and X is the projection of the separation distance between the centres of the colliding drops normal to the relative velocity vector and gives a measure of the degree to which the collision is off-centre.

For near head-on collisions with increasing We, the impact can result in permanent coalescence, bouncing, permanent coalescence again and temporal coalescence followed by reflexive separation into two or more drops. In particular, for equal-sized water drops colliding head-on in one atmosphere air, reflexive separation into two drops may first occur at $We = 19$ [12]. This limit has been found to depend on the liquid and surrounding gas pressure. For instance, Qian and Law [14] report limits of $We \sim 20$–40 for hydrocarbon droplets colliding in gas environments at different pressures, while Menchaca-Rocha et al. [15] found even higher critical values ($We \geqslant 80$) for mercury drops colliding in atmospheric air. As We is further increased, reflexive separation may result in a string of three or more drops. The reader is referred to the review article by Orme [16] for a complete discussion of the experimental data for both water and fuel drop collisions. Further experiments conducted by Willis and Orme [17,18] have shown that for 10- and 30-cSt oil drops colliding head-on in a vacuum environment, the collisions always resulted in permanent coalescence for We up to about 350 and 2840, respectively, which are on the order of 10–100 times higher than the critical value for water drop collisions in a standard atmosphere. It is believed that this increase in the critical Weber number is due to the fact that there is no air pressure to aerodynamically disrupt the thin films or ligaments generated in the collision.

In general, for off-centre and grazing collisions four distinct types of outcome have been categorized, namely permanent coalescence and bouncing at low and moderate We, reflexive separation for higher We and low impact parameters ($\leqslant 0.4$) and stretching separation for both higher We and higher impact parameters. In general, when two liquid drops of comparable size collide nearly head-on, they coalesce to form a transient circular disk-like drop which then contracts radially. The radial influx is driven by the surface tension forces and pushes the liquid out of the disk centre, forming a long cylinder of rounded ends. As We is increased, a critical point is reached beyond which the liquid cylinder breaks up into two drops. This critical point marks the onset of the type of collision outcome called reflexive or influx separation. Conversely, when two drops collide off-centre at high impact parameters, only a portion of them comes in direct contact, resulting in a well-defined region of interaction. As the bulk of the drops tend to flow in the direction of their initial trajectory, the region of interaction stretches. If either We or the impact parameter is increased, the ratio of the drop kinetic energy, which tries to stretch and separate the combined mass, over the surface energy of the interaction region, which tries to hold the two drops together, also increases until a critical value is achieved beyond which stretching separation occurs. In the latter case, as the impact parameter is further increased, the stretched interaction region connecting the two receding drops may eventually break up into one or more satellite droplets [12]. In passing, we recall that head-on and off-centre binary collisions with very high relative velocities may result in shattering separation in which the colliding drops disintegrate into a cluster of much smaller droplets.

In spite of the wealth of existing experimental results, numerical simulations aimed at studying the dynamics of the collision and coalescence of liquid drops are indeed very scarce. A first attempt to simulate the head-on collision of equal-sized water drops for $We < 5$, using the marker-and-cell method, was reported by Foote [19]. Further numerical studies were made by Poo and Ashgriz [20], who employed a volume-of-fluid scheme to follow the dynamics of binary drop collision in two-space dimensions (2D). Simulations of the head-on collision of two drops were also carried out by Nobari et al. [21], who used a front tracking method to investigate the boundary separating the occurrence of bouncing and permanent coalescence. A brief report on the numerical simulation of drop collisions was published by Rieber and Frohn [22], which mainly discusses the numerical techniques and does not provide much details on the collision behaviour. Mashayek et al. [23] studied the axisymmetric coalescence produced by the collision of two liquid drops using a Galerkin finite element method in combination with the spine-flux scheme for tracking the free surface. In particular, they investigated

the effects of varying Reynolds number (Re), impact velocity, drop size ratio and internal circulation on binary coalescence for low $We(\approx 1)$. More recently, Inamuro et al. [24] applied a lattice Boltzmann multiphase method to simulate the binary collision of liquid drops in ambient gas at $Re = 2000$ for $20 < We < 80$ and varied impact parameters. In particular, they studied the occurrence of permanent coalescence, reflexive separation for low impact parameters and stretching separation for high impact parameters.

Here, we apply for the first time the method of smoothed particle hydrodynamics (SPH) to simulate the collision dynamics and coalescence of equal-sized van der Waals liquid drops in 2D planar geometry. Therefore, the simulations apply to the coalescence of two infinitely long cylinders. In particular, we study how the shape of the coalesced cylindrical drops evolves with time and compare the evolution with that observed in actual experiments involving the collision and coalescence of spherical drops. In common with Mashayek et al. [23], we consider only low impact energy collisions with $We \leqslant 10$ in a vacuum environment. In contrast with them, we include in a self-consistent manner the effects of bulk viscosity, viscous heating and heat conduction, and allow for both head-on and off-centre binary collisions. Since SPH is a grid-free method, the results will be independent of any prescribed coordinate system compared to previous finite difference and finite element based simulations. This makes SPH a scheme suitable to follow large surface deformations as in problems involving free surface [25] and interfacial [26,27] flows. Here, we show that when SPH is coupled with the allowance for molecular cohesive forces through a van der Waals equation of state, free surfaces and gas–liquid interfaces can be handled in a natural manner without the need of either using free-surface tracking methods [28] or by-hand inclusion of the surface tension forces in the equations of motion along with specialized expressions for calculating the location of the interface and determining its curvature [26,27].

2. Basic formulation and methodology

The general equations describing the motion of a heat conducting, viscous fluid can be written using the standard index-summation convention as

$$\frac{\mathrm{d}\rho}{\mathrm{d}t} + \rho\frac{\partial v^k}{\partial x^k} = 0, \tag{2}$$

$$\rho\frac{\mathrm{d}v^i}{\mathrm{d}t} = \frac{\partial S^{ij}}{\partial x^j} \tag{3}$$

and

$$\rho\frac{\mathrm{d}u}{\mathrm{d}t} = S^{ij}\frac{\partial v^i}{\partial x^j} - \frac{\partial q^k}{\partial x^k}, \tag{4}$$

where ρ is the mass-density, v^i is the ith component of the fluid velocity, u is the specific internal energy, S^{ij} are the components of the stress tensor, q^k is the kth component of the heat flux and x^j is the jth Cartesian component of the position vector $\vec{r}$. Here, $\mathrm{d}/\mathrm{d}t = \partial/\partial t + v^i\partial/\partial x^i$ denotes the Lagrangian time derivative. The stress tensor is defined according to

$$S^{ij} = -p\delta^{ij} + \sigma^{ij}, \tag{5}$$

where p is the internal pressure, δ^{ij} is the unit tensor and σ^{ij} is the viscous stress tensor given by

$$\sigma^{ij} = \eta\left(\frac{\partial v^i}{\partial x^j} + \frac{\partial v^j}{\partial x^i}\right) + \left(\zeta - \frac{2}{d}\eta\right)\frac{\partial v^k}{\partial x^k}\delta^{ij}, \tag{6}$$

with η and ζ being the coefficients of shear and bulk viscosity, respectively. The constant parameter d specifies the number of spatial dimensions, with $d = 2$ for two dimensions and $d = 3$ for three dimensions. The heat flux is assumed to obey Fourier's law of heat conduction and is given by

$$q^k = -\kappa\frac{\partial T}{\partial x^k}, \tag{7}$$

where κ is the coefficient of thermal conductivity and T is the fluid temperature. For a van der Waals fluid model, Eqs. (2)–(4) are closed by the constitutive relations

$$p = \frac{\bar{k}_\mathrm{B}\rho T}{1 - \bar{b}\rho} - \bar{a}\rho^2 \tag{8}$$

and

$$u = \frac{\xi}{2}\bar{k}_\mathrm{B}T - \bar{a}\rho, \tag{9}$$

for the pressure and specific internal energy, respectively. In these equations, ξ is the number of degrees of freedom for the molecules, $\bar{k}_\mathrm{B} = k_\mathrm{B}/m$, $\bar{b} = b/m$ and $\bar{a} = a/m^2$, where k_B is the Boltzmann's constant, b is a constant due to the finite volume of the molecules, a is a measure for the forces of cohesion between neighbouring molecules and m is the mass of the molecules. Here, we take $\xi = 2$, corresponding to spherical molecules that are allowed to move only in the (x, y)-plane. Note that for any inner volume element the cohesive forces approximately cancel each other because they are on average directionally uniform. However, the same is not true for a volume element adjacent to the surface, where they add up to a resultant pressure in the direction of the inward surface normal. It is precisely this contribution which is responsible for the capillarity of the free liquid surface. In this model, thermo-dynamic stability demands that the inequalities

$$\bar{k}_\mathrm{B}T > 2\bar{a}\rho(1 - \bar{b}\rho)^2 \tag{10}$$

and

$$\rho < \frac{1}{\bar{b}} \tag{11}$$

must be satisfied. The first inequality ensures that the specific heats, the isentropic bulk modulus, $K_s = \rho(\partial p/\partial\rho)_s$, and the product between the thermal expansion coefficient (α) and the Grüneisen coefficient (Γ),

$$\alpha\Gamma = -\frac{1}{\rho^2}\left(\frac{\partial\rho}{\partial T}\right)_p\left(\frac{\partial p}{\partial u}\right)_\rho,$$

are all positive quantities. The second inequality guarantees that the kinetic pressure, given by the first term on the right-hand side of Eq. (8), is always positive. The combination of these constraints along with the positiveness of the density, ρ, temperature, T, and Grüneisen coefficient, Γ, define the domain of the phase space for this van der Waals fluid model.

The SPH formalism used for solving Eqs. (2)–(4) is described in full by Sigalotti et al. [29] and Meleán et al. [30]. Here, we present only a brief description of the method, and refer the reader to the above papers for more details. SPH is a fully Lagrangian particle method used for computation of discontinuous flows with large deformations. In addition to Eqs. (2)–(4), it also solves the equation

$$\frac{\mathrm{d}x^i}{\mathrm{d}t} = v^i \tag{12}$$

for the particle's position. The formal discretization of Eqs. (2)–(4) is obtained through the use of an interpolating kernel function that gives the estimate of the field variables at a set of points (or particles) suitably chosen to represent the fluid elements. In practice, mean values of a quantity are expressed by the convolution integral of the quantity with the kernel function, which is then approximated as a sum over neighbouring points. For instance, the density at each particle's location is simply assigned by

$$\rho_a = \sum_{b=1}^{N} m_b W_{ab}, \tag{13}$$

where the subscripts denote particle labels, m_b is the mass of particle b, $W_{ab} = W(|\vec{r}_a - \vec{r}_b|, h)$ is a spherically symmetric interpolating kernel, h is the parameter of the kernel or smoothing length which determines the spatial resolution and the sum is taken over N neighbouring particles within a circle of radius $2h$. Eq. (13) is effectively a second-order approximation to Eq. (2) and its use is of normal practice in standard SPH. With the use of Eq. (13) to evaluate the density, the SPH representations of Eqs. (3) and (4) must be written in symmetrized form to guarantee variational consistency [29,31]. In this way, momentum preservation can be addressed properly. In this variationally consistent SPH formulation, the expressions for the viscous forces on the right-hand side of Eq. (3) involve only first-order derivatives of the kernel through a straightforward evaluation of the components of the viscous stress tensor. This allows the use of low-order kernels of compact support such as the cubic spline kernel originally proposed by Monaghan and Lattanzio [32], without the occurrence of significant instability.

The position, velocity and specific internal energy of the particles are advanced in time from step n to step $n+1$ in a two-stage procedure according to a modified leapfrog integrator, which is accurate to second-order in the timestep $\Delta t = t^{n+1} - t^n$. In the first stage, a predicted estimate for particle 'a' is obtained at the intermediate time $t^{n+1/2}$ using the following sequence:

$$\begin{aligned}
\vec{x}_a^{\,n+1/2} &= \vec{x}_a^{\,n-1/2} + \Delta t\vec{v}_a^{\,n},\\
\vec{v}_a^{\,n+1/2} &= \vec{v}_a^{\,n} + \frac{1}{2}\Delta t\left(\frac{\mathrm{d}\vec{v}}{\mathrm{d}t}\right)_a^n,\\
u_a^{n+1/2} &= u_a^n + \frac{1}{2}\Delta t\left(\frac{\mathrm{d}u}{\mathrm{d}t}\right)_a^n.
\end{aligned} \tag{14}$$

The values of $\vec{x}_a^{\,n+1/2}$ are then used in Eq. (13) to get the time-centred density, $\rho_a^{n+1/2}$, which in turn allows the temperature to be updated using the $u_a^{n+1/2}$ in Eq. (9). Finally, the time-centred pressure is obtained by direct evaluation of Eq. (8) with ρ and T replaced by $\rho_a^{n+1/2}$ and $T_a^{n+1/2}$, respectively. These predicted estimates are then employed to compute the time-centred acceleration, $(\mathrm{d}\vec{v}/\mathrm{d}t)_a^{n+1/2}$, along with the viscous and heat conduction contributions to the time rate of change of the specific internal energy, $(\mathrm{d}u/\mathrm{d}t)_a^{n+1/2}$. In the second stage, final updates of the particle's positions, velocities and specific internal energies are obtained as follows:

$$\begin{aligned}
\vec{x}_a^{\,n+1} &= \vec{x}_a^{\,n} + \Delta t\vec{v}_a^{\,n+1/2},\\
\vec{v}_a^{\,n+1} &= \vec{v}_a^{\,n} + \Delta t\left(\frac{\mathrm{d}\vec{v}}{\mathrm{d}t}\right)_a^{n+1/2},\\
u_a^{n+1} &= u_a^n + \Delta t\left(\frac{\mathrm{d}u}{\mathrm{d}t}\right)_a^{n+1/2},
\end{aligned} \tag{15}$$

from which updated densities, temperatures and pressures are computed from Eqs. (13), (9) and (8), respectively. For SPH particles, the timestep in the above explicit scheme is limited by the Courant condition for numerical stability [34]. However, for the model calculations of this paper accurate results were obtained using a constant value of $\Delta t(=0.005)$, which was chosen to be as small as necessary to guarantee stability.

The present scheme has been proved to perform equally well for compressible flows at moderate and high Re and incompressible flows at very low $Re(\ll 1)$ without resorting to any trick or modification [29]. Further testing of the method on the formation of a stable van der Waals liquid drop has shown that it is highly susceptible to unstable behaviour in the tensile regime. Specifically, for this particular test case the tensile instability appears in the form of unphysical concentric ring-like clusterings of particles in the structure of the forming drop [30]. However, the instability is completely removed by add-

ing an artificial viscous force and energy heating term to the SPH equations of motion and internal energy according to the prescriptions given by Gray et al. [33]. Complete details of the form of the artificial stress and corrected SPH equations can be found in Meleán et al. [30].

3. Liquid drop and binary collision models

In this paper, we perform exploratory SPH calculations of the binary collision and subsequent coalescence of infinitely long cylindrical drops of equal radius. The colliding drops are assumed to be physically identical and in thermo-mechanical equilibrium. The drop model configuration is constructed numerically by adopting the same parameters used by Nugent and Posch [35] and Meleán et al. [30]. That is, we take $m = 1$, $\bar{a} = 2$, $\bar{b} = 0.5$ and $\bar{k}_B = 1$ in Eqs. (8) and (9). These reduced units leads to a van der Waals fluid whose critical point occurs for $\rho_{cr} = 2/3$, $p_{cr} = 8/27$ and $T_{cr} = 32/27$ [36]. When written in terms of the reduced variables $\rho \to \rho/\rho_{cr}$, $p \to p/p_{cr}$ and $T \to T/T_{cr}$, Eq. (8) expresses the law of corresponding states, that is, it contains only the above reduced variables and not quantities pertaining to a given substance [36]. It is therefore valid for any fluid to which Eq. (8) is applicable. In other words, the reduced isotherms are the same for all substances. The coefficients of thermal conductivity, shear and bulk viscosity in reduced units are taken to be $\kappa = 5$, $\eta = 1$ and $\zeta = 0.1$, respectively. This large value of κ serves to obtain a fast temperature adjustment, reducing density fluctuations in the drop. In addition, a value of $\eta = 1$ corresponds to a liquid with moderate viscosity [35]. We choose the (x, y)-plane to represent the fluid and start the evolution from a square array of 1936 SPH particles, of equal mass ($m_a = m = 1$), placed at the vertices of a regular square Cartesian mesh of total side length $L_m = 32.25$. With this choice, the interparticle distance along the x- and y-directions is 0.75. The particles were given a smoothing length $h = 3$ and an initial uniform temperature $T = 0.2$. At this subcritical value, a condensed circular drop with no external atmosphere is formed as shown in Fig. 1(a).

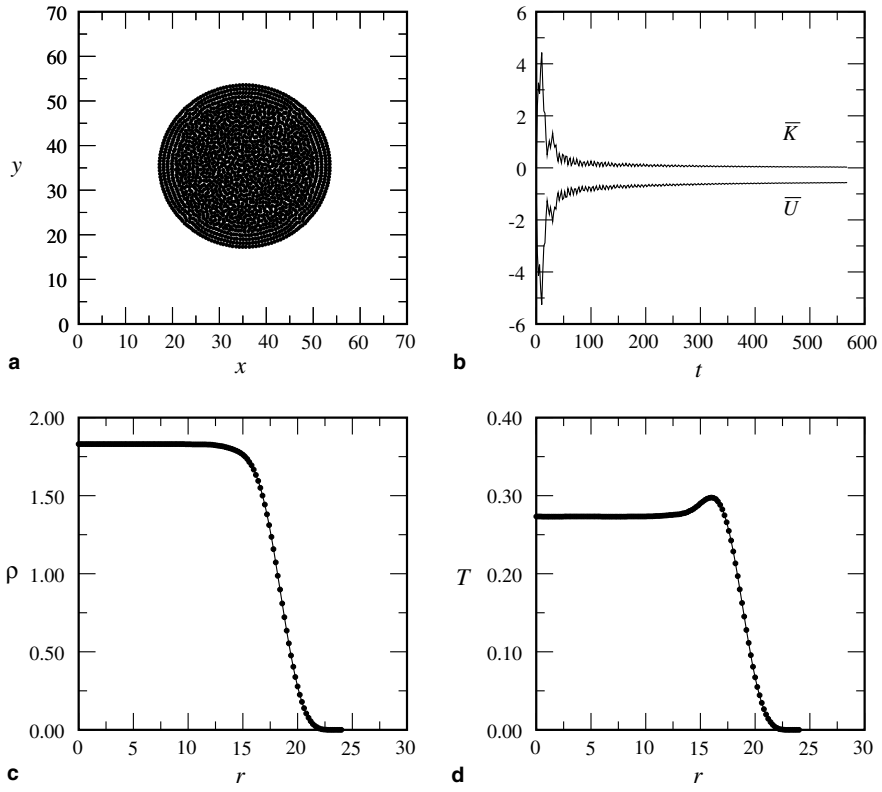

Fig. 1. (a) Stable circular drop configuration used for the binary collision models, (b) time variation of the kinetic (K) and internal (U) energies within the drop during the evolution leading to the equilibrium configuration shown in (a), (c) SPH-smoothed mass-density and (d) temperature variations as functions of the distance r from the centre of mass for the stable drop in (a). For convenience $\bar{K} = K/10$ and $\bar{U} = (U + 6000)/10$ are plotted instead of K and U in (b). All quantities are in reduced units.

As in Nugent and Posch [35], surface tension effects at the drop boundary are simulated by considering the cohesive pressure, $-\bar{a}\rho^2$, in Eq. (8) separately from all other forces. This term contributes with an attractive central force between the SPH particles and produces an acceleration and heating given by

$$\frac{\mathrm{d}\vec{v}_a}{\mathrm{d}t} = 2\bar{a}\sum_{b=1}^{N} m_b \nabla_a W_{ab}^H \tag{16}$$

and

$$\frac{\mathrm{d}u_a}{\mathrm{d}t} = 2\bar{a}\sum_{b=1}^{N} m_b(\vec{v}_b - \vec{v}_a)\cdot\nabla_a W_{ab}^H, \tag{17}$$

respectively, where ∇_a is the gradient operator at the location $\vec{r}_a$ of particle 'a' and $W_{ab}^H = W(|\vec{r}_a - \vec{r}_b|, H)$ is the same interpolating kernel function employed in Eq. (13), except that it now depends on the smoothing range H instead of h. We note that the form of Eq. (16) strongly resembles that employed to estimate the surface normals for calculating interfacial curvatures with SPH using the continuum-surface-force method [26]. The choice of H is determined by stability considerations. In particular, stable and circular drops, as the one depicted in Fig. 1(a), are produced when $H \geqslant 2h$, that is, when the interaction range of the attractive cohesive forces is assumed to exceed that of all other smoothed forces appearing in the SPH equations of motion. A similar observation also led to a substantial improvement of the interface stability properties with the continuum-surface-force method employed by Morris [26]. The forces represented by Eq. (16) largely cancel within the drop volume, except for a small strip H around the drop surface where particles are accelerated in the direction of the inward surface normal. In this way, the right-hand side of Eq. (16) acts as a net surface tension force due to the local curvature. Its main effect is to smooth out regions of high curvature in an attempt to reduce the total surface area and hence the surface energy.

Also displayed in Fig. 1 is the time variation of the internal kinetic (K) and internal (U) energy during the evolution leading to the formation of the stable drop (Fig. 1(b)) and the smoothed density (Fig. 1(c)) and temperature (Fig. 1(d)) profiles for the final equilibrium drop shown in Fig. 1(a). The circular shape of the stable drop is one effect of the rising surface tension, σ, due to the pressure difference at the interface separating the liquid drop from the surrounding vacuum. The circularly ordered outermost particles evident in Fig. 1(a) illustrate the finite thickness of the interface surrounding the drop. The drop has a central density $\rho_c \approx 1.8$ and radius $R \approx 18.2$ in reduced units. With these parameters we may then compute σ using Laplace formula

$$|p(r=0) - p(r\to\infty)| = \frac{\sigma}{R}, \tag{18}$$

where $p(r = 0)$ and $p(r \to \infty) = 0$ are the pressures in the drop centre and far away from it, respectively. Since $p(r = 0) \approx -0.39$ for this drop, Laplace formula yields $\sigma \approx 7.1$. With these parameters, the Ohnesorge number, $Z = 16\eta/(\rho R\sigma)^{1/2}$, representing the ratio of the viscous force to the square root of the product of the inertial and surface tension forces is $Z \approx 1.05$ for this drop model.

Following Ashgriz and Poo [12], a model of binary drop collision can be described by the liquid-drop density ρ, the shear viscosity η, the surface tension σ, the diameters D_1 and D_2 of the colliding drops and their relative velocity $\vec{v}_{\mathrm{rel}} = \vec{v}_1 - \vec{v}_2$. For simplicity, here we consider only collisions between equal-sized drops ($D_1 = D_2 = D$) for which $|\vec{v}_1| = |\vec{v}_2| = v$, where v is assumed to be a constant. From the above fluid parameters we can construct the three dimensionless numbers (i.e., Re, We and χ) that characterize the binary drop collision as defined by Eq. (1). Since the (x, y)-plane is used to represent the colliding drops, the calculations apply to the coalescence of two infinitely long cylinders. The initial geometry for both the head-on and off-centre collision models proposed here is shown schematically in Fig. 2. The relative motion of the drops is described in the reference frame in which one of them is at rest. In this frame, the other drop will approach the one at rest with a reference velocity equal to the relative velocity $v_{\mathrm{rel}} = 2v$ as measured in the centre-of-mass system. Computationally, this is accomplished by adding an initial constant axial velocity v_{rel} to the internal liquid velocity field of the incident drop. As depicted in Fig. 2(a), a head-on collision refers to the case in which the relative velocity vector coincides with the centre-to-centre line (here chosen in the direction of the x-axis), yielding $X = 0$ and hence $\chi = 0$. A simple off-centre collision model is obtained by shifting the centre of the inci-

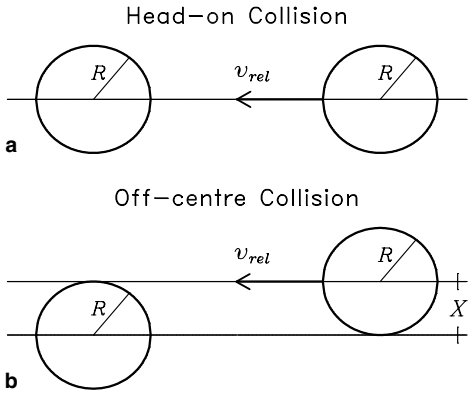

Fig. 2. Schematic of (a) the head-on and (b) off-centre binary collision models as viewed in the reference frame in which one of the two drops is at rest. The symbols used in this figure are as defined in the text.

dent drop in the vertical direction a distance equal to its radius R, resulting in a dimensionless impact parameter $\chi = 0.5$ (Fig. 2(b)). In this particular geometry the collision angle is identically zero, implying that for any given choice of the reference velocity, v_{rel}, both the head-on and off-centre binary drop collision models will be characterized by the same values of Re and We. Two sequences of seven model calculations each, corresponding to $\chi = 0$ and 0.5, respectively, are defined by taking values of $v_{rel} \approx 0.360$, 0.468, 0.573, 0.662, 0.811, 0.936 and 1.047, which are appropriate for low energy impact collisions with $1.2 \leqslant We \leqslant 10.1$ and $23.5 \leqslant Re \leqslant 68.4$.

4. Head-on binary collision

For $1.2 \leqslant We \leqslant 10.1$, all head-on collision models resulted in permanent coalescence of the impinging drops. We recall that in general two drops will coalesce if their minimum clearance distance reaches a critical value which is within the range of the intermolecular forces of the fluid, typically of the order of 100 Å [6]. However, it is well known that low We head-on collisions may also lead to bouncing, a mechanism in which direct contact is prevented by the gas film between the drop interfaces [14]. In contrast with most practical situations, the present exploratory model calculations refer only to collisions of liquid drops in a vacuum environment (i.e., with zero outer gas pressure) and so we cannot expect the drops to bounce. This agrees with the experimental observation that as the surrounding gas pressure is decreased in low We head-on collisions of liquid drops, the outcome of bouncing is suppressed because the pressure buildup within the interdrop film is consequently reduced, thus easing rapid drainage of the film and favouring coalescence [14]. In addition, the drops are thermally insulated. That is, there is no heat conduction through the drop surface into the vacuum because there the thermal conductivity is exactly zero.

In vacuum, where there is no interdrop film, the incident drops find no way to lose their translational velocities before contact is established. As a consequence, they come together, reaching a minimum clearance on their centre-to-centre line and experiencing negligible hydrodynamic deformation upon contact, regardless of the impact inertia. When the drops touch, the surface tension forces drive a flow into the point of contact to form a tiny liquid bridge. This very early phase is depicted in Fig. 3 for the $We \approx 10$ head-on collision model. The first slide (at $t = 10$) shows the precise instant when the drops touch and the bridge is formed, followed by its subsequent broadening at $t = 12$ and 14 (second and third slides, respectively). Notice that all head-on models start with the drops separated a distance approximately half their radius R and so the time of contact t_c will differ from model to model depending on the size of the relative velocity.

The results for this early phase can be compared with the analytical asymptotic solutions for drop coalescence derived by Hopper [37] and Eggers et al. [38]. In particular, Hopper [37] provided a 2D solution for the coalescence of two infinitely long cylinders. For the special case in which the outer fluid is inviscid or absent, he found that the radius of the small bridge, as measured in the direction normal to the centre-to-centre line, varies with time according to

$$r_m \sim \frac{\sigma(t - t_c)}{\pi\eta} \ln\left[\frac{\sigma(t - t_c)}{\eta R}\right] \tag{19}$$

and that the flow is driven by a highly curved 'meniscus' of length $2\pi r_m$ and width $\Delta \sim r_m^3$ around the bridge, while the fluid velocity at the meniscus obeys a logarithmic dependence on radius given by

$$v_m \sim -\frac{\sigma}{\pi\eta} \ln\left(\frac{r_m}{R}\right). \tag{20}$$

Eggers et al. [38] extended Hopper's analysis to the coalescence of two spherical drops. Since the flow within the bridge is driven by the curved meniscus, they found that during the early stage of coalescence, the result should be asymptotically the same as in 2D and hence Eqs. (19) and (20) should equally apply. Eq. (19) is an asymptotic statement for $t - t_c \to 0$, where t refers to

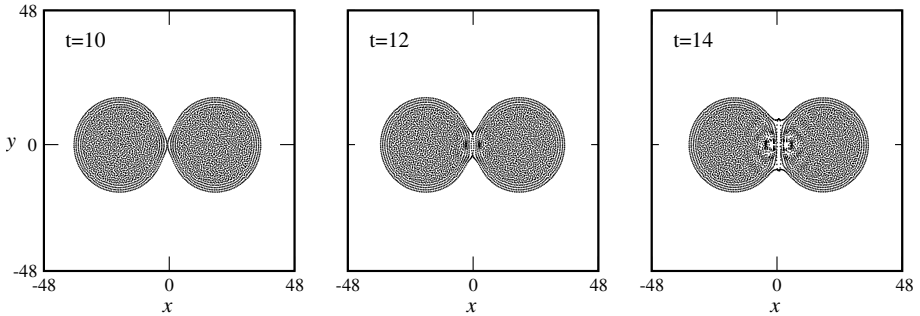

Fig. 3. Early evolution of the head-on collision model with $v_{rel} \approx 1.047$ ($We \approx 10$), showing the liquid bridge formed between the drops immediately after contact and its subsequent broadening. In each slide the time is shown in reduced units.

the evolution time and t_c, as defined above, is the time of drop contact. Its validity rests on the conservative assumption that the scale $\Delta \sim r_m^3$ is smaller than r_m so that the force almost exclusively comes from the meniscus. Fig. 4 compares the analytical solution given by Eq. (19) with the numerically predicted behaviour of $r_m(t)$ for all head-on models. In particular, the best fits with the analytical solution are obtained when $r_m \leqslant 0.11R$ for the low energy collision models with $v_{rel} \approx 0.360$ ($We \approx 1.2$) and 0.468 ($We \approx 2$). At small radii ($r_m \to 0$), the Reynolds number, $Re = \rho\sigma r_m/\eta^2$, is arbitrarily small. This together with the large velocity gradients generated near the meniscus makes the motion there to be always dominated by viscous effects. This flow takes place on a time scale given by $\tau = \eta R/\sigma \approx 2.56$ in reduced units, which compares fairly well with the time required by r_m to become as large as ≈0.26 (for $We \approx 1.2$) to ≈0.52 (for $We \approx 10$) times the radius of the parent drops (see Fig. 4). The bridge broadens at a faster rate in collisions with higher impact velocities because of their larger associated Re collision values. For $r_m > 0.11R$, the numerically calculated $r_m(t)$ differs from Eq. (19). The reason for this is that Eq. (19) is valid only for drops having negligible velocities of approach before contact [38]. In fact, Eq. (20) predicts that $v_m \to 0$ when $r_m \to R$, which complies with the expectation that in the absence of sustained internal motion within the combined drop, the free surface can adjust the flow to lessen the velocity gradients and hinder further motion of the surface when $r_m \sim R$.

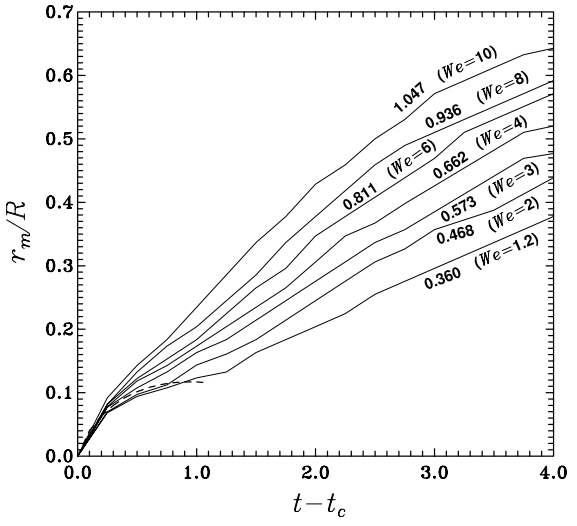

Fig. 4. Time growth of the bridge radius r_m for all head-on collision models compared with the asymptotic analytic solution (dashed line) given by Eq. (19). The numbers on the curves refer to the relative velocity of collision and the corresponding value of the Weber number to which they belong. All quantities are in reduced units.

In a recent paper, Yao et al. [39] measured the growth of the bridge at the onset of coalescence of two highly viscous, silicon oil drops immersed in a water–alcohol mixture of the same density in order to avoid the effects of gravity. They found that for times t/τ larger than about 0.1, where $\tau = \eta R/\sigma$, the bridge radius varies with time according to the scaling formula $r_m = Rf(t/\tau)$, where f is some function, while the fluid velocity at the meniscus varies linearly with r_m. However, they did not provide experimental data at sufficiently small times ($t/\tau \ll 0.1$) and so a direct comparison with the analytical solution predicted by Eqs. (19) and (20) was not possible. In addition, their experiments apply to the viscously dominated limit in which $Z \gg 1$ and hence their results cannot be compared with those in Fig. 4, which applies to drops with $Z \sim 1$.

The details of the long-term evolution up to completion of the first period of oscillation are displayed in Figs. 5 and 6 for the $v_{rel} \approx 0.468$ ($We \approx 2$) and 1.047 ($We \approx 10$) models, respectively. Both models evolve in a qualitatively similar fashion in spite of the difference in their We values. In either case, as long as $r_m \approx R$ the bulk of the drops merges. During this stage, nearly half of the translational kinetic energy of the incident drop is converted into internal motion, while the other part, which is of the same magnitude of the centre-of-mass kinetic energy before the collision, goes as translational motion of the combined drop. The former results in two opposite flows within the coalescing drop directed towards the central plane perpendicular to the x-axis. As a consequence, a 'stagnation-flow' region forms around this plane in as much as the same way as described by Jiang et al. [13]. The pressure within this region soon exceeds the surface tension pressure, causing an outwardly spreading flow along the y-axis. As this motion progresses, the overall width of the coalesced drop reduces with a consequent increase of the rim pressure. This phase of the evolution is depicted in the top-row slides of Figs. 5 and 6 for the time intervals $28 \leqslant t \leqslant 114$ and $18 \leqslant t \leqslant 86$, respectively. The outward motion seen in the present simulations is the analogous of the outwardly radial flow envisaged in actual liquid-drop collision experiments, which leads to the formation of a transient dimpled disk [13,14,17,18]. The developed disk stage corresponds to the elongated shapes displayed in the last slide of top row in Figs. 5 ($t = 114$) and 6 ($t = 86$). These slides clearly show the combined drop in their largest surface deformation.

The dynamics during this phase of the evolution is governed by rather strong viscous dissipation. From a simple energy balance analysis, Jiang et al. [13] inferred that about half of the internal kinetic energy is lost towards the stage of maximum deformation (see Section 6). Since the magnitudes of the internal velocities change quicker along the y-axis due to the higher surface energies involved, fluid motion undergoes stronger viscous

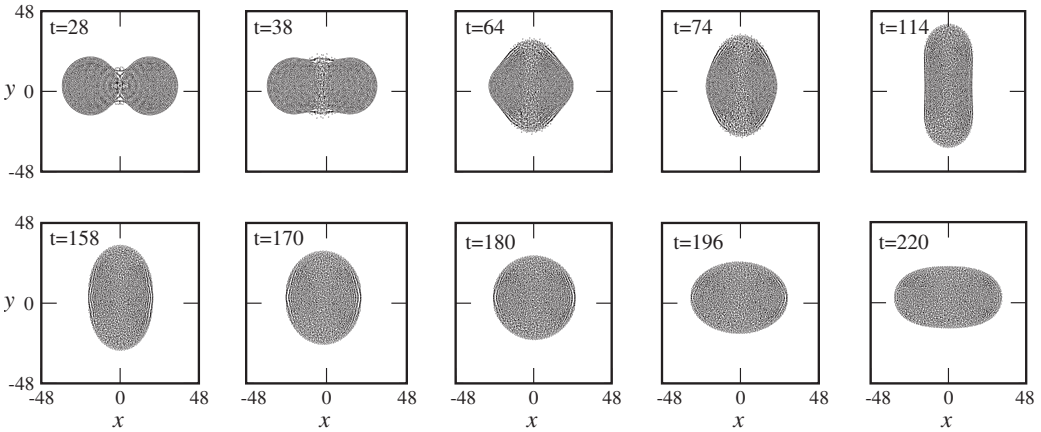

Fig. 5. Sequence of times showing the evolution of the head-on collision model with $v_{rel} \approx 0.468$ ($We \approx 2$). In each slide the evolution time is shown in reduced units.

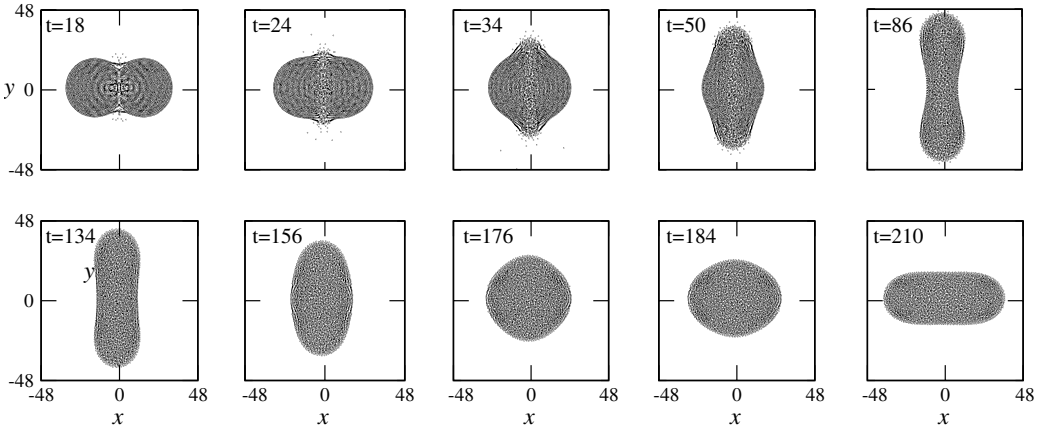

Fig. 6. Sequence of times showing the evolution of the head-on collision model with $v_{rel} \approx 1.047$ ($We \approx 10$). In each slide the evolution time is shown in reduced units.

dissipation in this direction than along the x-axis. The model of Fig. 6, with $We \approx 10$ and $Re \approx 68$, formed a thinner disk compared to that of Fig. 5 having lower $We(\approx 2)$ and $Re(\approx 31)$ collision values. Also, note that for the former model the disk possesses well-pronounced concave surfaces on each side around the centre-to-centre line of the parent drops. Due to the higher initial kinetic energy for this case, the surface around the centre-to-centre line continues to move inwards until a concave surface is formed which then produces adverse pressures that prevent further inward motion of the surface. This result is in close agreement with previous simulations by Mashayek et al. [23] with the aid of different numerical techniques, who found that higher collision values of Re translate into larger surface deformation.

Development of the disk ceases as soon as the rim pressure first balances and then overcomes the stagnation pressure, causing the disk to contract back under surface tension. The bottom-row slides of Figs. 5 and 6 show the reverse motion of the surface towards completion of the first oscillation period. In particular, the last slides in Figs. 5 ($t = 220$) and 6 ($t = 210$) depict the shape of the coalesced drops close to the end of the first period by the time the maximum elongation happens to be along the x-axis. These forms correspond to the stretched liquid cylinder detected in drop collision experiments after the disk contraction phase. As in Mashayek et al. [23], we also find that higher Re collision values result in more elongated coalesced drops by the end of the first period of oscillation. The subsequent evolution will be governed by a long-term interplay between viscous dissipation and conversion into surface energy of the internal liquid movement, with a consequent damped oscillatory motion with maximal

drop elongations alternating between being parallel and perpendicular to the direction of incidence. This phase will eventually end with the formation of a circular coalesced drop.

Fig. 7 depicts the velocity field within the combined drop at four distinct times in the sequence of Fig. 6, as viewed in the reference frame in which one of the pre-collision drops is at rest (see Fig. 2(a)). In this frame, half of the translational kinetic energy of the incident drop is transformed into internal motion, while the other half remains in the form of translational motion of the combined mass as a whole. The top left panel in Fig. 7 shows the flow structure at $t = 34$, when most of the kinetic energy is still confined in the bulk of the incident drop (right-hand cap). At this time, the maximum velocity is $\approx 1.076 v_{\rm rel}$. A region of flow transition forms around the $x = 0$ plane, where in the central part the x-directed flow velocity changes from $\sim v_{\rm rel}$ in the right-hand cap to almost zero in the left-hand cap and an outwardly directed flow develops along the y-axis in the top and bottom extremes of the end caps. The latter flow is responsible for the further expansion of the drop towards the point of largest deformation. This transition region is the equivalent of the 'stagnation-flow' region that forms because of a counterflow directed towards the $x = 0$ plane, as seen in the reference frame in which the centre of mass of the colliding drops is at rest. The description of the counterflow can be recovered from the flow pattern in the top left panel of Fig. 7 by simply adding the constant velocity $\frac{1}{2} v_{\rm rel}$ to the negative x-component of the particle velocities. The top right panel at $t = 86$ shows the velocity field close to the point of maximum deformation. At this time, the velocity vectors point to the left and are all nearly aligned with the x-axis, indicating the translational motion ($v \sim 0.5 v_{\rm rel}$) of the combined drop. The maximum and minimum velocities are $\approx 0.62 v_{\rm rel}$ and $\approx 0.46 v_{\rm rel}$, implying that most of the undamped internal kinetic energy has been effectively converted into surface energy. The bottom panels (at $t = 156$ and 176) pertains to the disk contraction phase. The inclined arrows in the top and bottom hemispheres show that there is sustained inward motion along the y-axis. Meantime, expansion of the drop occurs primarily about the $y = 0$ plane, where the main flow is along the x-direction. In the centre-of-mass frame, this flow will take the form of two opposite flows along the positive and negative x-directions away from the drop centre.

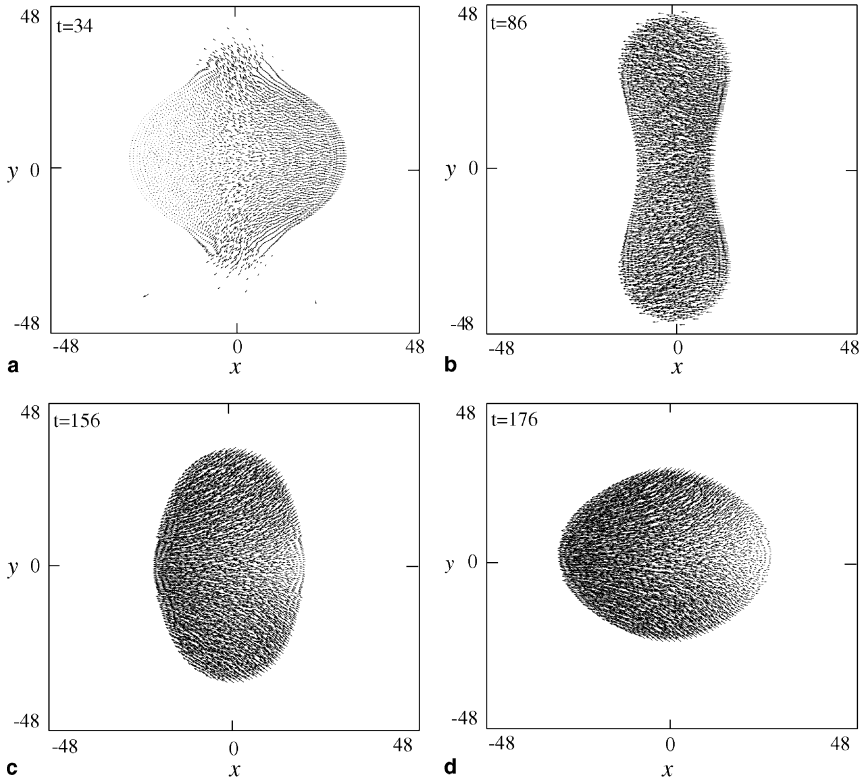

Fig. 7. Velocity field at $t = 34$ (top left), $t = 86$ (top right), $t = 156$ (bottom left) and $t = 176$ (bottom right) for the head-on collision model of Fig. 6, as viewed in the reference frame in which one of the two colliding drops is at rest. The maximum velocity within the coalesced drop is $v_{\rm max} \approx 1.076 v_{\rm rel}$ (top left), $v_{\rm max} \approx 0.62 v_{\rm rel}$ (top right), $v_{\rm max} \approx 0.85 v_{\rm rel}$ (bottom left) and $v_{\rm max} \approx 0.90 v_{\rm rel}$ (bottom right).

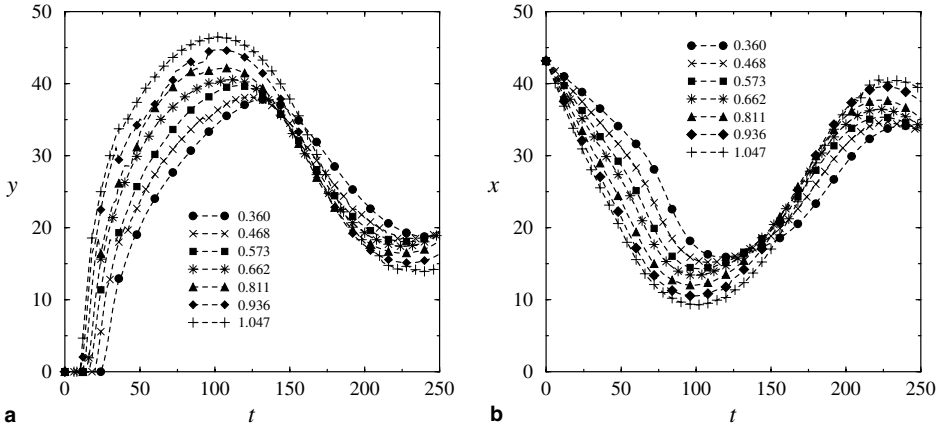

Fig. 8. Motion of a surface particle located on (a) the y-axis and (b) x-axis for all head-on collision models. The symbols marking the curves identify the relative velocity to which they belong.

In order to describe the form of the oscillations due to the drop surface deformation, we choose a planar coordinate system (x, y) and place it within the drop by fixing its origin at the location of the drop centre-of-mass. In this way, the surface deformation can be followed by tracking the motion of those surface particles which are closest to the x- and y-axes. The motion of these particles along the y- and x-axes is shown in Fig. 8(a) and (b), respectively, for all head-on models. It is clear from Fig. 8(a) that the higher energy collisions reach the stage of largest deformation on shorter times and with larger oscillation amplitudes than the lower energy models. Larger amplitudes are also seen to occur along the x-axis for the higher velocity impacts (Fig. 8(b)), implying that the more energetic is the collision, the thinner is the shape of the combined drop at maximum deformation and the more elongated will appear after completion of the first period. This result is consistent with the higher energy impacts pointing towards higher We and Re collision values. We also note that due to viscous loss of the internal kinetic energy, the maximum elongations along the x-axis (at the end of the first period) are always smaller than those undergone by the drops along the y-axis at the time of largest deformation.

5. Off-centre binary collision

In this section, we describe the results obtained for the evolution of the off-centre collision models for $1.2 \leqslant We \leqslant 10.1$ and dimensionless impact parameter $\chi = 0.5$, as shown in Fig. 2(b). We may see from Fig. 9 that at the precise instant when the drops touch, their centre-to-centre line forms an angle with the direction of the relative velocity vector given by $\sin\theta = \chi$. Hence, the components of the relative velocity parallel and normal to the centre-to-centre line can be readily calculated as $v_l = (1 - \chi^2)^{1/2} v_{rel}$ and $v_t = \chi v_{rel}$, respectively. Thus, for $\chi = 0.5$, the longitudinal velocity is $v_l \approx 0.87 v_{rel}$, while the transverse one is exactly half the magnitude of the relative velocity. According to the experimental observations of Jiang et al. [13], the longitudinal component is responsible for the coalescence and subsequent deformation of the combined drop into a plate shape in a manner similar to the head-on case, while the transverse velocity causes a sliding motion of the impacting masses and enforces rotational motion of the coalesced drop as a whole. Since in the present models motion is constrained on the (x, y)-plane, the combined drop will rotate about a stable axis normal to the plane and coinciding with its centre of mass.

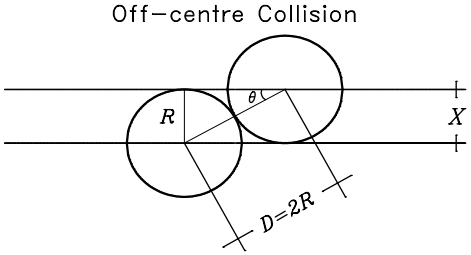

Fig. 9. Schematic of the off-centre binary collision at the time of contact, showing the angle ($\sin\theta = X/D = \chi$) formed by the centre-to-centre line and the direction of approach.

Figs. 10 and 11 display a sequence of slides for the time evolution of the off-centre binary collision models when $v_{rel} \approx 0.468$ ($We \approx 2$) and 1.047 ($We \approx 10$), respectively, so that direct comparison can be made with the head-on evolutions of Figs. 5 and 6. During the initial phase, a bridge between the drops forms again at the point of contact, which then expands in radius in as much as the same way as described for the head-on

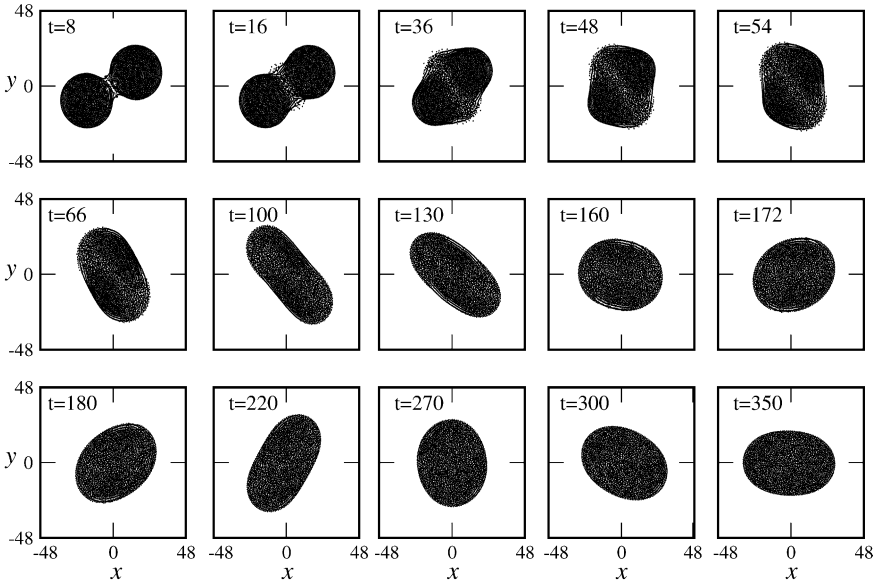

Fig. 10. Sequence of times showing the evolution of the off-centre collision model with $v_{rel} \approx 0.468$ ($We \approx 2$). In each slide the evolution time is shown in reduced units.

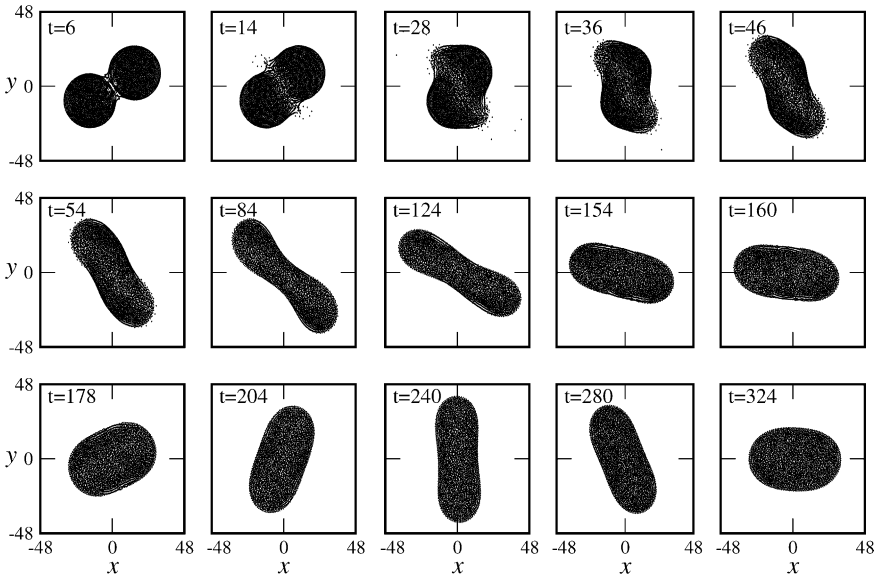

Fig. 11. Sequence of times showing the evolution of the off-centre collision model with $v_{rel} \approx 1.047$ ($We \approx 10$). In each slide the evolution time is shown in reduced units.

collisions. As the drops merge, half of the longitudinal kinetic energy carried by the incident drop is converted into internal motion of the fluid in the form of a counterflow (see Section 6). This results in the rapid formation of a stagnation-flow region around the central plane perpendicular to the centre-to-centre line, which separates the bulk of the coalescing masses. The transverse velocity causes these masses to slide about the stagnation plane in opposite directions in an attempt to break the bridging between them, as shown in the three last slides of top row in Figs. 10 and 11, where deformation into a 'peanut' mode is already evident. Development of the peanut shape is more clearly seen in Fig. 11 because of the stronger transverse inertial forces for

the $We \approx 10$ case. While part of the sliding motion is resisted by viscous forces due to the shearing flow layer between the sliding masses, part is transformed into rotational motion by the action of the surface tension forces which tend to circularize the drop. The centrifugal forces associated with rotation of the deforming end caps sandwiching the stagnation region along with the outwardly accelerated flow within it, induced by the initial kinetic energy pertaining to the longitudinal velocity, flatten the combined drop until a stage of maximum deformation is reached. This point is achieved at $t = 100$ in the low $We(\approx 2)$ collision (Fig. 10) and $t = 84$ for $We \approx 10$ (Fig. 11), as shown in each figure by the second slide of middle row. Note that because of the larger momentum effects associated with the latter case, the peanut shape has undergone transition into a rotating dumb-bell mode. A common feature in all models is that due to the elongated shapes, the centrifugal forces first induce 'solid-body' rotation of the coalesced drop about its centre of mass.

The top left and right panels of Fig. 12 show the details of the flow at $t = 36$ and 46, respectively, in the evolution sequence of Fig. 11. As in the head-on case (Fig. 7), the internal flow is shown in the reference frame in which one of the colliding drops is at rest (see Fig. 2(b)). At these times, the maximum velocity is $\approx 1.08 v_{\mathrm{rel}}$ with most of the initial kinetic energy being confined in the top portion of the combined mass, which contains the bulk of the incident drop. A region of flow transition, which separates the bulks of the coalescing drops, is again present in which strong velocity gradients develop as a result of the coalescence process. Note that the flow velocity is higher in the top end caps, while the converse is true in the bottom end caps. This marked difference in the velocity is responsible for enforcing solid-body rotation as the combined drop elongates (see Fig. 11). In particular, the bottom left panel (at $t = 124$) of Fig. 12 displays the velocity field close to the point of maximum elongation, when $v_{\max} \approx 0.73 v_{\mathrm{rel}}$ and $v_{\min} \approx 0.26 v_{\mathrm{rel}}$. At this point, the drop has completed half of a revolution period and most of the internal longitudinal motion has either dissipated or gone into surface energy, while most of the internal transverse motion (with velocity $\sim 0.25 v_{\mathrm{rel}}$) is in the form of solid-body rotation, as is clearly evidenced by the flow pattern. In this way, the combined drop undergoes translational motion in a direction parallel to the centre- to-centre line at the time of contact (see Fig. 9), while revolving about an axis

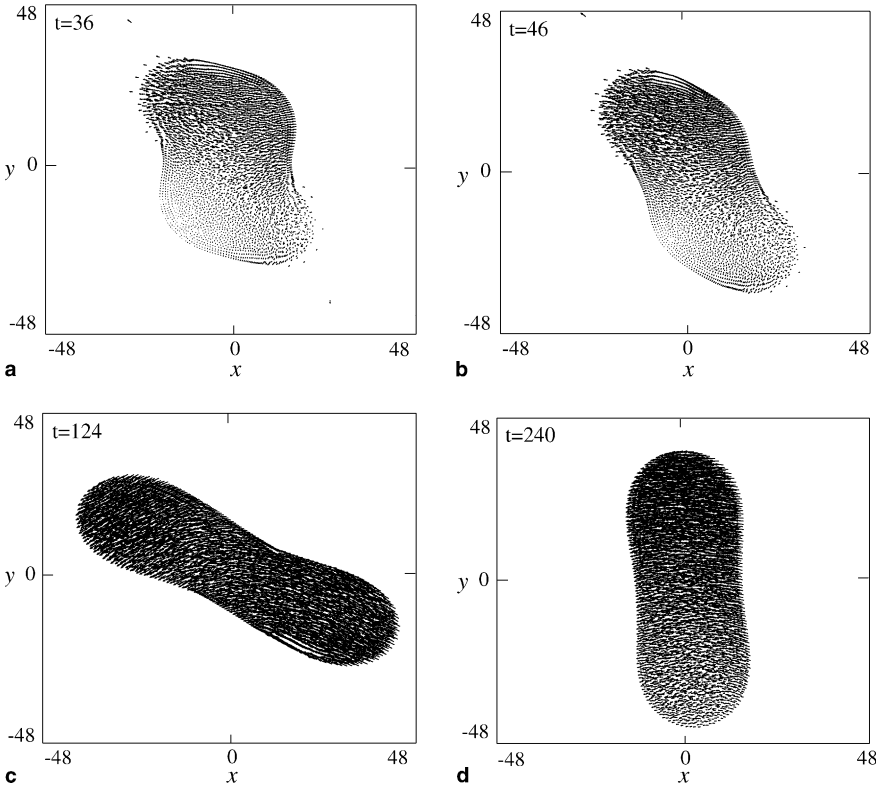

Fig. 12. Velocity field at $t = 36$ (top left), $t = 46$ (top right), $t = 124$ (bottom left) and $t = 240$ (bottom right) for the off-centre collision model of Fig. 11, as viewed in the reference frame in which one of the two colliding drops is at rest. The maximum velocity within the coalesced drop is $v_{\max} \approx 1.082 v_{\mathrm{rel}}$ (top left), $v_{\max} \approx 1.078 v_{\mathrm{rel}}$ (top right), $v_{\max} \approx 0.73 v_{\mathrm{rel}}$ (bottom left) and $v_{\max} \approx 0.71 v_{\mathrm{rel}}$ (bottom right).

passing through its centre of mass. Further evidence of this rotational motion is given in the bottom right panel of Fig. 12 at $t = 240$, when the drop has already completed a full revolution period.

As in the head-on case, drop elongation is halted by the overwhelming surface tension forces which then pull the flow back, making the rotating coalesced drop to oscillate longitudinally for the remainder of the evolution. The amplitudes of this vibrational mode progressively decay as the internal fluid motion is viscously dissipated. By about $t = 180$ (Fig. 10) and 178 (Fig. 11) when the drops have completed a full revolution, transition to an almost circular shape has occurred. This mode is the analogous of the oblate shape attained in real liquid-drop experiments. Evidently, the surface reflex flow is much stronger in the $We \approx 10$ model, where rapid deformation of the oblate shape into an elongated prolate one is seen to occur at $t = 240$ (Fig. 11). This elongation would correspond to the stretched cylinders observed in actual experiments. The subsequent longitudinal vibrations will damp out due to both viscous dissipation and conversion of the internal motion into surface energy, until a spinning spherical blob is formed. In passing, we note that during the initial phase of coalescence before the stage of largest deformation, the internal velocity gradients involved are large enough to make viscous dissipation to be essentially independent of the coefficient of shear viscosity, η. However, after the point of maximum elongation the velocity gradients associated with the surface reflex flow are considerably smaller and so loss of the internal kinetic energy depends more strongly on the rheological properties of the fluid through the coefficients of surface tension and shear viscosity. In the transition towards sphericity both viscous and surface tension forces also contribute to damping of the angular momentum (see Section 6). As the coalesced drop becomes circular, the rotational motion appears in the form of spin angular momentum of the blob about its axis of symmetry. Shearing motion between adjacent rotating layers will then ultimately contribute to further damping of rotation by viscous dissipation.

The longitudinal oscillations of the coalesced drop have been monitored by following the drop surface motion in a frame co-rotating with the liquid. The results of this motion are similar to those displayed in Fig. 8(a) and (b) for the head-on models, except that in this case the amplitudes of the oscillations are smaller.

6. Energy dissipation

The collision of two liquid drops is a perfectly inelastic process in which the drops combine to form a bigger one. In the reference frame in which one of the drops is at rest (Fig. 2), the total (translational plus internal) kinetic energy before the collision is simply $K_0 = \frac{1}{2}Mv_{\rm rel}^2 + 2K_{\rm int,0}$, where M is the mass of the incident drop and $K_{\rm int,0}$ is the kinetic energy due to the internal macroscopic motion. In all models considered here the initial drop configuration is close to mechanical equilibrium (see Fig. 1(b)) and therefore $K_{\rm int,0} \ll \frac{1}{2}Mv_{\rm rel}^2$. After a head-on collision, the combined drop undergoes translational motion in the direction of incidence with a velocity ($\frac{1}{2}v_{\rm rel}$) equal to that of the centre of mass before the impact. Therefore, the total kinetic energy after the collision is $K = \frac{1}{4}Mv_{\rm rel}^2 + K_{\rm int}$, where $K_{\rm int}$ is the amount of the translational kinetic energy which is transformed into internal motion. Conservation of the total energy then yields

$$K_{\rm int} + U = \frac{1}{4}Mv_{\rm rel}^2 + 2(K_{\rm int,0} + U_0), \tag{21}$$

where U_0 and U are, respectively, the internal energy before and after the collision. Since the right-hand side of Eq. (21) is a constant, $\mathrm{d}(K_{\rm int} + U)/\mathrm{d}t = 0$, implying that any change in $K_{\rm int}$ must be balanced by a corresponding opposite change in U. Under the assumption of fluid incompressibility ($\partial v^k/\partial x^k = 0$), Eqs. (2)–(4) can be written as

$$\frac{\mathrm{d}K_{\rm int}}{\mathrm{d}t} = -\frac{1}{2}\eta\int\left(\frac{\partial v^i}{\partial x^j} + \frac{\partial v^j}{\partial x^i}\right)^2(\mathrm{d}x)^d - \oint p\vec{v}\cdot\vec{n}(\mathrm{d}x)^{d-1} + \oint(\vec{v}\cdot\vec{\sigma})\cdot\vec{n}(\mathrm{d}x)^{d-1}, \tag{22}$$

$$\frac{\mathrm{d}U}{\mathrm{d}t} = \frac{1}{2}\eta\int\left(\frac{\partial v^i}{\partial x^j} + \frac{\partial v^j}{\partial x^i}\right)^2(\mathrm{d}x)^d - \oint \kappa\nabla T\cdot\vec{n}(\mathrm{d}x)^{d-1}, \tag{23}$$

where in two-space dimensions $d = 2$ and $\vec{n}$ is a unit vector normal to the surface (contour) bounding the liquid drop. The first two integrals on the right-hand sides of Eqs. (22) and (23) show that the internal kinetic energy lost per unit time due to viscous dissipation in the bulk of the drop is converted into heat. The surface integral in the second term of Eq. (22) is the work done by pressure forces on the liquid within the free surface. It accounts for the conversion of the internal kinetic energy into surface tension energy and vice versa. The surface integrals in the last terms of Eqs. (22) and (23) represent the time variations of the internal kinetic and specific internal energies due to internal friction and heat conduction within the free surface, respectively.

In the present simulations, the total energy before and after the collision is very well conserved, implying that the surface integrals in Eqs. (22) and (23) must approximately balance. Fig. 13(a) and (b) displays the time evolution of the total kinetic (K) and total internal (U) energy, respectively, for the head-on collision models. Since the translational kinetic energy of the combined drop ($\frac{1}{4}Mv_{\rm rel}^2$) is a constant, the time variation of K as shown in Fig. 13(a) reflects the actual time varia-

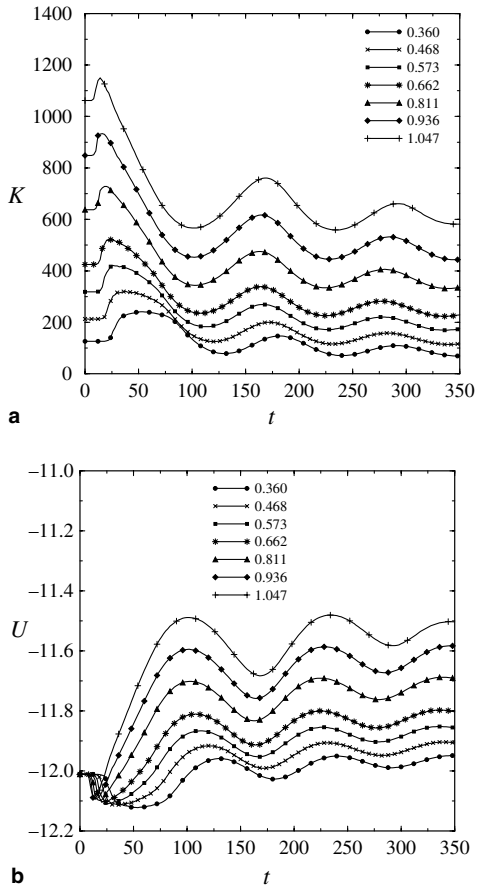

Fig. 13. Time evolution of (a) the total kinetic and (b) internal energy for all head-on collision models. The symbols marking the curves identify the relative velocity of collision to which they belong. All quantities are in reduced units.

tion of the internal kinetic energy $K_{\rm int}$. When the drops reach a minimum clearance distance, their surfaces around the point of contact slightly deform due to the cohesive forces between nearby fluid molecules. As a result a tiny bridge connecting the drops forms. During this initial stage (see Fig. 3), the highly curved meniscus around the bridge drives a rapid flow in the direction perpendicular to the centre-to-centre line, making the bridge to broaden and the kinetic energy to rise steeply over its constant value, K_0, before the collision (Fig. 13(a)). Because of the large velocity gradients generated within the expanding bridge, the rate of increase of K soon slows down due to the overwhelming effects of viscous dissipation. This leads to a maximum in K. At this point the contribution of the first and third terms of Eq. (22) is balanced by that of the second term and so $\mathrm{d}K_{\rm int}/\mathrm{d}t = 0$ momentarily.

The converse occurs for the internal energy which drops steeply reaching a minimum value (Fig. 13(b)). The time scale for viscous heating due to internal friction within the bridge ($\tau_{\rm vis} \sim \rho u r_{\rm m}^2/2\eta v_{\rm m}^2$) is much longer than the conducting time ($\tau_{\rm con} \sim \rho u r_{\rm m}^2/\kappa T_{\rm m}$). Choosing $v_{\rm m}$ and $T_{\rm m}$ as appropriate mean values of the velocity and temperature at a time before the occurrence of the maximum in K, we obtain that $\tau_{\rm con}/\tau_{\rm vis} \leqslant 0.015$. Thus, heat is conducted away from the bridge region faster than it is being produced by internal friction, leading to a steep decrease of the internal energy. The maxima in Fig. 13(a) correspond to increments of the total kinetic energy ranging from ~8% (for $We \approx 10$) to ~92% (for $We \approx 1.2$) of the constant value, K_0, before the collision. However, the size of the increments ($\Delta K = K_{\max} - K_0$) has only a weak dependence on the impact inertia. In particular, $\Delta K \approx 115$ for $We \approx 1.2$ and $\Delta K \approx 88$ for $We \approx 10$. In the $We \approx 10$ collision model, the maximum in K occurs when the radius of the bridge is $r_{\rm m} \approx 0.58R$ (third slide of Fig. 3 at $t = 14$), while in the $We \approx 2$ case it happens when $r_{\rm m} \approx R$ (second slide of Fig. 5 at $t = 38$). In addition, we note that the widths of the 'uphill' and 'downhill' peaks in K and U, respectively, decrease for head-on collisions with higher We as a result of the higher Re collision values associated with them.

In all models, as long as $r_{\rm m} \sim R$, further outward motion of the combined drop surface along the y-axis is accompanied by inward motion of the surface along the x-axis. During this phase, the rapid drop of the kinetic energy is primarily caused by viscous dissipation within and around the stagnation region. In particular, the mean of the y-velocity component increases monotonically until it reaches a maximum value, which in reduced units, is between ≈0.17 (for $We \approx 1.2$) and ≈0.29 (for $We \approx 10$) by the time about 13% and 25% of the total kinetic energy has been lost, respectively. Thereafter, the mean y-velocity decreases almost linearly in time until it vanishes. At this point, most of the undamped internal motion has been changed into surface energy and so the kinetic energy reaches a minimum as seen in Fig. 13(a). In this process the internal energy increases as a result of the excess heating produced by the internal friction in the bulk and near the free surface of the drop (Fig. 13(b)). From Eq. (23) we may see that part of this heating is balanced by heat conduction, thus causing the rate of increase of the internal energy to slow down and vanish at the same time when K reaches its minimum value. This point marks the state of maximum drop deformation seen in the last slide of top row in Figs. 5 and 6. At this time the rim pressure which is of the order of σ/b, where b is the length of the drop along its elongation, balances the stagnation pressure ($K_{\rm int}$). More than half of the total kinetic energy is lost towards this stage (~67% for $We \approx 1.2$ and ~51% for $We \approx 10$). This result is consistent with the estimate of 50% loss predicted by Jiang et al. [13] through a simple energy balance analysis. In particular, most of the viscous loss occurs within

the stagnation region (along the y-axis) where the velocity gradients are larger (see the top left panel of Fig. 7). Only a small amount of viscous dissipation is indeed involved in the spreading rim region because there the free surface can adjust the flow to lessen the velocity gradients, especially for large values of the velocity. Also, note that heat conduction works all the way to equalize the temperature within the drop. This explains why the mean drop temperature rises only mildly during the evolution, while the internal energy increases towards the point of largest deformation, where it reaches a maximum.

As soon as the rim pressure exceeds the stagnation pressure, the surface tension forces drive a reflex flow which causes the drop to contract back along the y-axis (see bottom panels of Fig. 7). As a consequence, the kinetic energy increases and reaches a new maximum by the time when the drop makes a transition to a nearly circular shape (see third slide of bottom row in Figs. 5 and 6). At this point the effective kinetic energy is from ~60% (for $We \approx 1.2$) to ~65% (for $We \approx 10$) of the corresponding value at the first maximum. During this stage, the internal energy decreases because thermal conduction proceeds faster than heat production by internal friction in the bulk. When the contribution of these concurring effects balance, U attains a minimum which again coincides with the appearance of a maximum in K. Thereafter, the drop departs from its circular shape and expands along the x-axis towards completion of the first period of oscillation (see last slide of bottom row in Figs. 5 and 6). At this time the increasing rim pressure halts further expansion of the drop and so the kinetic energy reaches a new minimum as opposed to the internal energy. During this stage from ~52% (for $We \approx 1.2$) to ~27% (for $We \approx 10$) of the kinetic energy is lost. The oscillatory behaviour of K and U will continue in time with progressively lower amplitudes until eventually $K_{\rm int} \to 0$, or equivalently $K \to \frac{1}{4}Mv_{\rm rel}^2$.

For the off-centre collision geometry shown in Fig. 2(b), the total kinetic energy before the collision can be written as $K_0 = K_{\rm l,0} + K_{\rm t,0} + K_{\rm int,0}$, where $K_{\rm l,0} = \frac{1}{2}M(1-\chi^2)v_{\rm rel}^2$ and $K_{\rm t,0} = \frac{1}{2}M\chi^2 v_{\rm rel}^2$ are, respectively, the longitudinal and transverse components of the translational kinetic energy carried by the incident drop. Note that $K_{\rm l,0} > K_{\rm t,0}$ for impact parameters $\chi < 1/\sqrt{2}$. For the particular case in which $\chi = 0.5$, we have that $K_{\rm l,0} = 3K_{\rm t,0}$. After the collision, the total kinetic energy is $K = \frac{1}{4}Mv_{\rm rel}^2 + K_{\rm int,l} + K_{\rm int,t}$, where $K_{\rm int,l}$ and $K_{\rm int,t}$ are initially the internal kinetic energies pertaining to the longitudinal and transverse (rotational) components of the velocity. Fig. 14(a) and (b) displays the time variation of the total longitudinal $[K_{\rm l} = \frac{1}{4}M(1-\chi^2)v_{\rm rel}^2 + K_{\rm int,l}]$ and transverse $(K_{\rm t} = \frac{1}{4}M\chi^2 v_{\rm rel}^2 + K_{\rm int,t})$ kinetic energies for the off-centre collision models. The time evolution of the internal energy is similar to that depicted in Fig. 13(b) for the head-on cases, and hence it will not be shown explicitly here. As before, since $\frac{1}{4}M(1-\chi^2)v_{\rm rel}^2$ and $\frac{1}{4}M\chi^2 v_{\rm rel}^2$ are constant, the time variations of $K_{\rm l}$ and $K_{\rm t}$ intrinsically reflects those of $K_{\rm int,l}$ and $K_{\rm int,t}$, respectively.

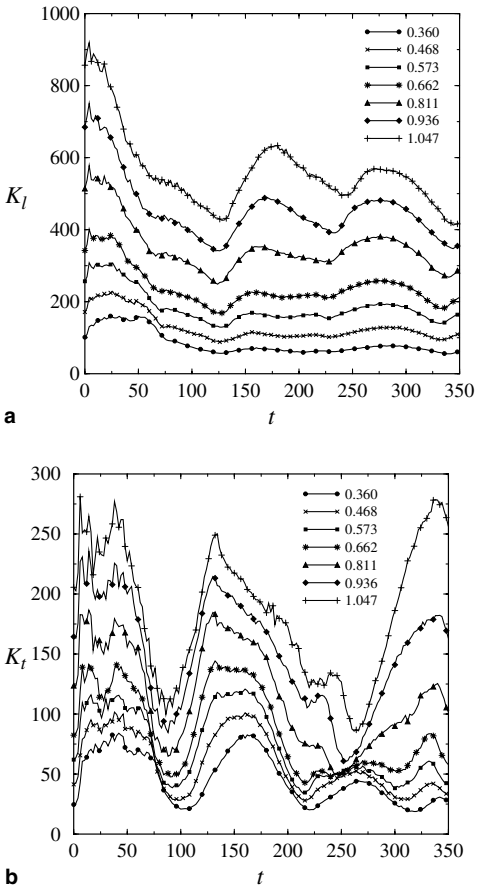

Fig. 14. Time evolution of (a) the total longitudinal and (b) transverse (rotational) kinetic energy for the off-centre collision models. The symbols marking the curves identify the relative velocity of collision to which they belong. All quantities are in reduced units.

A comparison of Figs. 13(a) and 14(a) clearly shows that the longitudinal kinetic energy in an off-centre collision varies with time in a qualitatively similar manner to the total kinetic energy in a head-on collision. This agrees with the experimental observations that the longitudinal component of the relative velocity is responsible for drop coalescence in as much as the same way as seen in a head-on collision [13]. However, the oscillations of $K_{\rm l}$ (Fig. 14(a)) and $K_{\rm t}$ (Fig. 14(b)) look much more irregular because of non-linear hydrodynamical coupling between the longitudinal and transverse (rotational) components of the internal motion. At the very beginning, the transverse kinetic energy rises steeply because of the rapid flow which develops within the expanding

bridge. When its radius becomes as large as that of the parent drops, viscous dissipation of the transverse motion makes K_t to stop rising and then oscillate by the time the drops undergo sliding motion about the stagnation plane (see slides of top row in Figs. 10 and 11). Thereafter, K_t decreases steeply because of the enhanced viscous dissipation due to shearing motion between the sliding masses and conversion of the transverse motion into surface tension. The increasing tensional forces halt further sliding motion and enforces solid-body rotation of the combined drop (see slides at $t = 54$ and 66 of Fig. 10, at $t = 46$ and 54 of Figs. 11 and 12). During this stage from ~75% ($We \approx 1.2$) to ~64% ($We \approx 10$) of K_t is effectively lost until a minimum is reached at the time of largest drop deformation, corresponding to the shapes shown at $t = 100$ in Fig. 10 and $t = 84$ in Fig. 11. Meanwhile, the longitudinal movement which is mainly responsible for the elongated shape is viscously dissipated at a slower rate because of the milder velocity gradients involved in the counterflow along the direction of the centre-to-centre line. A decrease from ~65% ($We \approx 1.2$) to ~54% ($We \approx 10$) in K_l is depicted in Fig. 14(a). The minima of K_l are slightly shifted in time with respect to those of K_t and approximately coincide with the shapes shown at $t = 130$ and 124 in Figs. 10 and 11, respectively. At this time in the evolution, the mean longitudinal velocity approximately vanishes implying that complete balance between the rim pressure and the stagnation pressure is achieved.

Starting from the first slide of middle row in Figs. 10 (at $t = 66$) and 11 (at $t = 54$), the time variation of K_t in Fig. 14(b) fits that of the rotational kinetic energy, while that in Fig. 14(a) gives the variation of the longitudinal (vibrational) component responsible for the alternating drop elongations. Note that around the point of largest elongation, the united drop experiences almost solid-body rotation about an axis perpendicular to the plane of the slides and coinciding with the drop centre-of-mass. This explains the further sudden rise of K_t for all models. In the meantime, the drop contracts back along its major axis with a consequent increase of K_l. Note that in the low We (<2) evolutions, the increase of K_l is only mild because most of the longitudinal motion has already been dissipated towards the stage of largest deformation. As a consequence, the further evolution is characterized by the drop undergoing mild elongations about a circular shape. In this way, most of the initial solid-body rotation is transformed into spin rotation of the drop. Viscous dissipation due to shearing motion between adjacent rotating layers causes the spinning to slow down, as shown in Fig. 14(b) by the lower oscillation amplitudes of K_t at long times for the $v_{rel} \leqslant 0.811$ ($We \leqslant 6$) models. The converse is true for the higher energy impacts ($v_{rel} \geqslant 0.936$ and $We \geqslant 8$), where the amplitudes of the oscillations remain almost undamped. This is a consequence of the stronger longitudinal inertial forces for the higher We cases, which make the coalesced drop to alternate between more elongated shapes. Therefore, only a little amount of the rotational energy is dissipated as the evolving drop experiences primarily solid-body rotation. In fact, the rate of change of the rotational energy increases just before and after the stages of largest elongation when the drop rotates almost rigidly (see Fig. 11). As long as it contracts back, making a transition to a circular shape before re-expanding, it passes through a sequence of less elongated shapes in which ~65% of the kinetic rotational energy is lost as the solid-body rotation goes into the form of spin. During drop contraction, part of the reflex flow is in the form of additional rotational motion. In particular, this additional rotational energy supplies most of the losses by viscous dissipation in the $v_{rel} \geqslant 0.936$ cases (see Fig. 14(b)). This result implies that dissipation of the rotational motion strongly depends on the impact inertia, and hence on the rate of dissipation of the longitudinal (vibrational) component of the velocity which determines the subsequent drop elongations.

7. Comparison with existing experimental and numerical results

There has been considerable effort to understand the events that occur when two drops collide. Most experimental work on the drop collision phenomena has been motivated by meteorological interest and applications to combustion spray systems. Therefore, attention has been focused on the collision behaviour of water drops at ambient pressures and hydrocarbon drops at both ambient and higher pressures. In addition, experiments of binary drop collision in a vacuum environment have been conducted by Willis and Orme [17,18]. Unlike experiments involving droplet collisions in a background medium, the later approach allows for studying the fluid dynamics of the collision decoupled from aerodynamic effects that would otherwise cause distortion or even disintegration of the coalesced mass. In particular, Willis and Orme [17,18] investigated the head-on binary collision of equal-sized, viscous drops with varied diameters and viscosities for Weber numbers in the range $355 < We < 4046$. Since the present calculations apply only to low We collisions, we cannot enforce direct comparison with their experimental results. However, the trends shown in the sequences of Figs. 5 (for $We \approx 2$) and 6 (for $We \approx 10$) up to $t = 180$ and 176, respectively, compare favourably well with their edge-on digital images of a binary collision sequence (see Fig. 5 of [17] and Fig. 6 of [18]) showing the coalesced drop deformation during the first half of the oscillation for a $We = 1560$ collision, where the combined drop deforms into a flat circular disk before relaxing into an approximate

spherical shape. The remainder of the drop evolution shown in Figs. 5 and 6 also reproduces the second half of the oscillation characterized by a prolate drop geometry (at $t = 220$ in Fig. 5 and 210 in Fig. 6), corresponding to the $t = t_{3\pi/2}$ time in the image sequences of [17,18]. As We is increased from ≈2 (Fig. 5) to ≈10 (Fig. 6), the magnitude of the maximum deformations (flat disk and prolate cylinder) increases monotonically, which is in agreement with the experimental observations of Willis and Orme [17,18]. In passing, we note that similar evolution shapes to those shown in Figs. 5 and 6 for the head-on collisions and in Figs. 10 and 11 for the off-centre collisions were also reported by Jiang et al. [13] and Qian and Law [14] in experiments involving the collision of water and hydrocarbon drops at atmospheric air.

In order to gain insight into the dynamics of the deformation process, we have also plotted in Fig. 8(a) and (b) the position of the spreading rim as a function of time for all head-on model calculations. In particular, Fig. 8(a) depicts the amplitude of deformation close to the y-axis. These curves are the analogous of those shown by Willis and Orme [18] for the radial expansion of the rim with time. Comparing Fig. 8(a) with their experimental curves reveals that the form of the oblate deformation cycle is relatively invariant with Weber number. As expected, higher deformation amplitudes correspond to more energetic collisions. For the low We collisions studied here, the maximum of the amplitude is shifted to the left as the Weber number is increased, implying that the deformed coalesced drop reaches the point of maximum deformation at slightly longer times in collisions with lower values of We. The experiments of Willis and Orme [18] show that as long as the Weber number is increased to very high values, the amplitude maxima occur at essentially the same time because of the increased inertial forces. The present calculations are also in good agreement with the linearly correlated experimental data obtained by Jiang et al. [13], which shows that about half of the pre-collision kinetic energy is lost in the deformation process towards the disk-like stage due to viscous dissipation and conversion of the internal motion into surface energy.

Previous theoretical and numerical investigations of drop behaviour have almost all been concerned with either the oscillations of a single drop or the collision of one drop with a flat wall. Numerical simulations of the collision of two drops are indeed very limited [20,21,23,24]. In particular, Nobari et al. [21] studied the head-on collision of equal-sized, axisymmetric drops immersed in an ambient fluid of much lower density and viscosity. They found that for varied Weber ($13 \leqslant We \leqslant 112$) and Reynolds ($28 \leqslant Re \leqslant 123$) numbers, the colliding drops always bounced because of the inability of their scheme to follow the rupture of the double interface upon drop contact. Only when rupture is allowed by artificially removing the double layer at prescribed times, do the drops coalesce permanently for $Re < 100$ regardless of the We value. Temporary coalescence followed by reflexive separation was obtained for $Re > 100$ provided that $We > 60$. For the lower We collisions, the shape evolution is very similar to that shown in Figs. 5 and 6. However, for fixed values of We and Re the extent of maximum deformation was seen to depend on the prescribed rupture times in the sense that the smaller is the rupture time, the thinner is the disk formed. In particular, for $We = 65$ and $Re = 140$ the predicted outcome is doubtful because when rupture is at an early time, the combined drop breaks up into two drops during its prolate regime, but when the rupture occurs at a later time permanent coalescence occurs. The head-on collision of equal- and non-equal-sized drops in a vacuum environment was studied by Mashayek et al. [23] for $We = 1$ and $3 \leqslant Re \leqslant 60$. In particular, the time resolved shape evolution for $Re = 30$ (see their Fig. 2(b)) strongly resembles that depicted in Fig. 5 for $We \approx 2$ and $Re \approx 31$. They found that for higher Re, the coalesced drop results in larger surface deformation during the oblate regime and in more elongated cylinders in the prolate cycle, as we can see by comparing their evolution with $Re = 60$ (their Fig. 2(c)) with Fig. 6 for $We \approx 10$ and $Re \approx 68$. However, because of the higher We for the evolution of Fig. 6, the surface around the centre-to-centre line at the point of largest deformation ($t = 86$) appears to be less concave at the expense of a more elongated shape compared to their Fig. 2(c) at $t = 1.270$. Also, the deformation amplitudes for different Reynolds numbers in their Fig. 3 compare reasonably well with those displayed in Fig. 8 for varied We and Re, implying that the form of the oscillations is more sensitive to variations of Re than to variations of We. In a more recent paper, Inamuro et al. [24] calculated the collision of two liquid drops in a gas phase at $Re = 2000$ for varied Weber numbers ($20 < We < 80$) and impact parameters ($0 \leqslant \chi < 0.82$). For the case in which $We = 20.2$ and $\chi = 0$, they obtained permanent coalescence following a shape evolution very similar to that shown in Fig. 6. Because of the rather large density ratio (=50) of the liquid to the ambient gas employed in their simulations, extrapolation of their results to lower values of We predicts an outcome of permanent coalescence regardless of the impact parameter, in good agreement with the results of the present calculations for an infinite density ratio. Although direct quantitative comparisons cannot be done with other existing simulations, several of the observed trends seem to be similar in spite of differences in the initial parameters and numerical techniques employed, implying that the SPH method is an alternative and promising numerical scheme for simulating the dynamics of colliding drops.

8. Conclusions

In this paper we have presented exploratory numerical simulations of the head-on and off-centre binary collision dynamics of equal-sized van der Waals liquid drops using the method of SPH. Only the outcome of coalescence for low energy impact collisions with Reynolds and Weber numbers in the ranges $23 \leqslant Re \leqslant 68$ and $1 \leqslant We \leqslant 10$, respectively, is studied. In particular, the effects of varying the relative velocity and the impact parameter ($\chi = 0$ for head-on and $\chi = 0.5$ for off-centre collisions) on permanent coalescence is investigated by following the oscillations of the combined drop configuration for more than a period.

The simulations apply to coalescence of two infinitely long cylindrical liquid drops in a vacuum environment. Therefore, their surfaces experience negligible hydrodynamic deformation upon contact, regardless of the impact inertia. When a minimum clearance distance is attained, a tiny liquid bridge connecting the incident drops and bounded on both sides by a highly curved surface, resembling a meniscus, suddenly forms. The high surface energy around the meniscus drives a rapid flow in the direction perpendicular to the centre-to-centre line which causes the bridge to broaden and the internal kinetic energy to rise steeply. For both the head-on and off-centre collision models studied here, the bridge broadens at a faster rate in collisions with higher *We* because of their higher associated values of *Re*. During this stage, the overwhelming viscous forces due to the large velocity gradients developed within the meniscus region soon balance the action of the surface tension forces. As a consequence, the kinetic energy stops rising and reaches a maximum value after which it starts decreasing. The increase of the kinetic energy is accompanied by a corresponding decrease of the internal energy. This occurs because the heat produced by internal friction within the bridge is efficiently fluxed by thermal conduction into the bulk of the coalescing drops. The balance of this concurrent effects makes the internal energy to achieve a minimum at exactly the same time when the internal kinetic energy reaches a maximum.

In all head-on collisions, when the radius of the bridge becomes as large as that of the incident drops, a stagnation-flow region forms about the bridging due to conversion of half of the translational kinetic energy into internal motion in the form of a counterflow. The pressure within this region soon exceeds the rim pressure, causing an outwardly spreading flow perpendicular to the direction of incidence. As a consequence, the combined drop elongates towards a state of maximum deformation, which is the exact analogous of the transient flattened disk observed in actual liquid-drop collision experiments. Towards this stage from $\sim$67% (for $We \approx 1$) to $\sim$51% (for $We \approx 10$) of the kinetic energy is lost by viscous dissipation and conversion of the internal motion into surface energy. The simulations also predict more elongated shapes after coalescence in collisions with higher impact inertia (higher *We* and *Re*), which complies with the results of previous simulations that higher collision values of *Re* translate into larger surface deformation. As the rim pressure exceeds the stagnation pressure, the surface tension forces drive a reflex flow which causes the drop to contract back and make a transition into a circular shape by the time the kinetic energy reaches a maximum. Further motion continues with the drop re-expanding along the direction of incidence towards a new stage of maximum elongation by the end of the first oscillation period. At this point the kinetic energy reaches a new minimum. The subsequent evolution will be governed by a long-term interplay between viscous dissipation and conversion of the internal liquid movement into surface energy, with a consequent damped oscillatory motion until a stable circular drop is formed.

In the present off-centre collision models, the value of the impact parameter ($\chi = 0.5$) is such that the magnitude of the longitudinal component of the translational kinetic energy is always three times larger than that of the transverse component. This occurs because the longitudinal component of the relative translational velocity is $\sqrt{3}$ times that of the transverse component for $\chi = 0.5$. In this way, the longitudinal component is primarily responsible for the coalescence and subsequent deformation of the combined drop into a plate shape as in the head-on collision models. As long as the bridge connecting the drops expands in radius, the transverse component causes the bulk of the coalescing drops to slide in opposite directions in an attempt to break the bridging between them. However, viscous dissipation due to shearing motion between the sliding masses helps the tensional bonding forces at the bridged part to resist the breaking and enforce centrifugal motion of the end caps of the coalescing drops. This results in solid-body rotation of the combined drop as it elongates. At the stage of maximum drop elongation, the models predict that from $\sim$65% (for $We \approx 1.2$) to $\sim$54% (for $We \approx 10$) of the longitudinal kinetic energy is lost. Dissipation of the rotational energy will strongly depend on the impact inertia. In particular, when $We \leqslant 6$ most of the longitudinal motion is dissipated towards the stage of maximum deformation thus leaving the drop to undergo only mild elongations about a circular shape towards completion of the first revolution period. In this process most of the solid-body rotation is changed into the form of spin rotation. Viscous dissipation due to shearing motion between adjacent rotating layers will ultimately damp out the rotational energy. Conversely, when $We \geqslant 8$ the combined drop oscillates while experiencing substantially more elongated shapes, thus favouring solid-body rotation and hence little dissipation of the

rotational motion. This result clearly implies that dissipation of rotation after coalescence in off-centre collisions strongly depends on the rate of dissipation of the longitudinal motion. Although the present calculations apply to the coalescence of two infinitely long cylinders, the predicted shape evolution during and after coalescence strongly resembles the edge-on images envisaged in real experiments involving the collision and coalescence of spherical drops.

Acknowledgements

We are truly indebted to the anonymous referees who have raised a number of suggestions and recommendations that have really improved the quality of the paper. This work is financially supported by the Instituto Venezolano de Investigaciones Científicas (IVIC).

References

[1] P.S. Shah, L.T. Fan, I.C. Kao, L.E. Erickson, Modeling of growth processes with two liquid phases: a review of drop phenomena, mixing, and growth, Adv. Appl. Microbiol. 15 (1972) 367–414.
[2] J.Y. Park, L.M. Blair, The effect of coalescence on drop size distribution in an agitated liquid–liquid dispersion, Chem. Eng. Sci. 30 (1975) 1057–1064.
[3] P.J. O'Rourke, F.V. Bracco, Modelling of drop interactions in thick sprays and a comparison with experiments, in: Stratified Charged Auto Engineering Conference, Institute of Mechanical Engineering Publications, 1980, pp. 101–116.
[4] S.R. Deshiikan, K.D. Papadopoulos, London–van der Waals and EDL effects in the coalescence of oil drops, J. Colloid Interface Sci. 174 (1995) 302–312.
[5] W.R. Cotton, R.A. Pielke, Human Impacts on Weather and Climate, Cambridge University Press, Cambridge, 1995.
[6] G.D.M. Mackay, S.G. Mason, The gravity approach and coalescence of fluid drops at liquid interfaces, Can. J. Chem. Eng. 41 (1963) 203–212.
[7] A.K. Chesters, The modelling of coalescence processes in fluid–liquid dispersions: a review of current understanding, Trans. Inst. Chem. Eng. 69 (A) (1991) 259–270.
[8] I.B. Ivanov, K.D. Danov, P.A. Kralchevsky, Flocculation and coalescence of micron-size emulsion droplets, Colloids Surf. A 152 (1999) 161–182.
[9] N. Ashgriz, P. Givi, Binary collision dynamics of fuel droplets, Int. J. Heat Fluid Flow 8 (1987) 205–210.
[10] N. Ashgriz, P. Givi, Coalescence efficiencies of fuel droplets in binary collisions, Int. Commun. Heat Mass Transfer 16 (1989) 11–20.
[11] G. Brenn, A. Frohn, Collision and merging of two equal droplets of propanol, Exp. Fluids 7 (1989) 441–446.
[12] N. Ashgriz, J.Y. Poo, Coalescence and separation of binary collisions of liquid drops, J. Fluid Mech. 221 (1990) 183–204.
[13] Y.J. Jiang, A. Umemura, C.K. Law, An experimental investigation on the collision of hydrocarbon droplets, J. Fluid Mech. 234 (1992) 171–190.
[14] J. Qian, C.K. Law, Regimes of coalescence and separation in droplet collision, J. Fluid Mech. 331 (1997) 59–80.
[15] A. Menchaca-Rocha, F. Huidobro, A. Martinez-Davalos, K. Michaelian, A. Perez, V. Rodriguez, N. Cârjan, Coalescence and fragmentation of colliding mercury drops, J. Fluid Mech. 346 (1997) 291–318.
[16] M. Orme, Experiments on droplet collisions, bounce, coalescence and disruption, Prog. Energy Combust. Sci. 23 (1997) 65–79.
[17] K.D. Willis, M.E. Orme, Experiments on the dynamics of droplet collisions in a vacuum, Exp. Fluids 29 (2000) 347–358.
[18] K.D. Willis, M.E. Orme, Binary droplet collisions in a vacuum environment: an experimental investigation on the role of viscosity, Exp. Fluids 34 (2003) 28–41.
[19] G.B. Foote, The water drop rebound problem dynamics of collision, J. Atmos. Res. 32 (1975) 390–401.
[20] J.Y. Poo, N. Ashgriz, Numerical simulation of collision of two-dimensional drops, in: Proceedings of the Fifth Annual Conference on Liquid Atomization and Spray Systems, San Ramon, CA, 1992, pp. 110–115.
[21] M.R.H. Nobari, Y.J. Jan, G. Tryggvason, Head-on collision of drops–A numerical investigation, Phys. Fluids 8 (1996) 29–42.
[22] M. Rieber, A. Frohn, Navier–Stokes simulations of droplet collision dynamics, in: Proceedings of the Seventh International Symposium on Computational Fluid Dynamics, Beijing, China, 1997, pp. 520–525.
[23] F. Mashayek, N. Ashgriz, W.J. Minkowycz, B. Shotorban, Coalescence collision of liquid drops, Int. J. Heat Mass Transfer 46 (2003) 77–89.
[24] T. Inamuro, S. Tajima, F. Ogino, Lattice Boltzmann simulation of droplet collision dynamics, Int. J. Heat Mass Transfer 47 (2004) 4649–4657.
[25] J.J. Monaghan, Simulating free surface flows with SPH, J. Comput. Phys. 110 (1994) 399–406.
[26] J.P. Morris, Simulating surface tension with smoothed particle hydrodynamics, Int. J. Numer. Meth. Fluids 33 (2000) 333–353.
[27] A. Colagrossi, M. Landrini, Numerical simulation of interfacial flows by smoothed particle hydrodynamics, J. Comput. Phys. 191 (2003) 448–475.
[28] F. Mashayek, N. Ashgriz, A spine-flux method for simulating free surface flows, J. Comput. Phys. 122 (1995) 367–379.
[29] L.Di.G. Sigalotti, J. Klapp, E. Sira, Y. Meleán, A. Hasmy, SPH simulations of time-dependent Poiseuille flow at low Reynolds numbers, J. Comput. Phys. 191 (2003) 622–638.
[30] Y. Meleán, L.Di.G. Sigalotti, A. Hasmy, On the SPH tensile instability in forming viscous liquid drops, Comput. Phys. Commun. 157 (2004) 191–200.
[31] J. Bonet, T.-S.L. Lok, Variational and momentum preservation aspects of smoothed particle hydrodynamic formulations, Comput. Meth. Applied Mech. Eng. 180 (1999) 97–115.
[32] J.J. Monaghan, J.C. Lattanzio, A refined particle method for astrophysical problems, Astron. Astrophys. 149 (1985) 135–143.
[33] J.P. Gray, J.J. Monaghan, R.P. Swift, SPH elastic dynamics, Comput. Meth. Applied Mech. Eng. 190 (2001) 6641–6662.

[34] L. Hernquist, N. Katz, TREESPH: a unification of SPH with the hierarchical tree method, Astrophys. J. Suppl. Ser. 70 (1989) 419–446.
[35] S. Nugent, H.A. Posch, Liquid drops and surface tension with smoothed particle applied mechanics, Phys. Rev. E 62 (2000) 4968–4975.
[36] L.D. Landau, E.M. LifshitzStatistical Physics, vol. 5, Addison-Wesley Publishing Company, Reading, MA, 1969, p. 270.
[37] R.W. Hopper, Plane Stokes flow driven by capillarity on a free surface, J. Fluid Mech. 213 (1990) 349–375.
[38] J. Eggers, J.R. Lister, H.A. Stone, Coalescence of liquid drops, J. Fluid Mech. 401 (1999) 293–310.
[39] W. Yao, H.J. Maris, P. Pennington, G.M. Seidel, Coalescence of viscous liquid drops, Phys. Rev. E 71 (2005) 016309-1–016309-5.